Supporting Information for

On the Feasibility of Depth Profiling of Animal Tissue by Ultrashort Pulse Laser Ablation

Slobodan Milasinovic, Yaoming Liu, Chhavi Bhardwaj, Melvin Blaze M.T., Robert J. Gordon and Luke Hanley*

Department of Chemistry, m/c 111, University of Illinois at Chicago, Chicago, IL 60607-7061

Further Experimental Details.

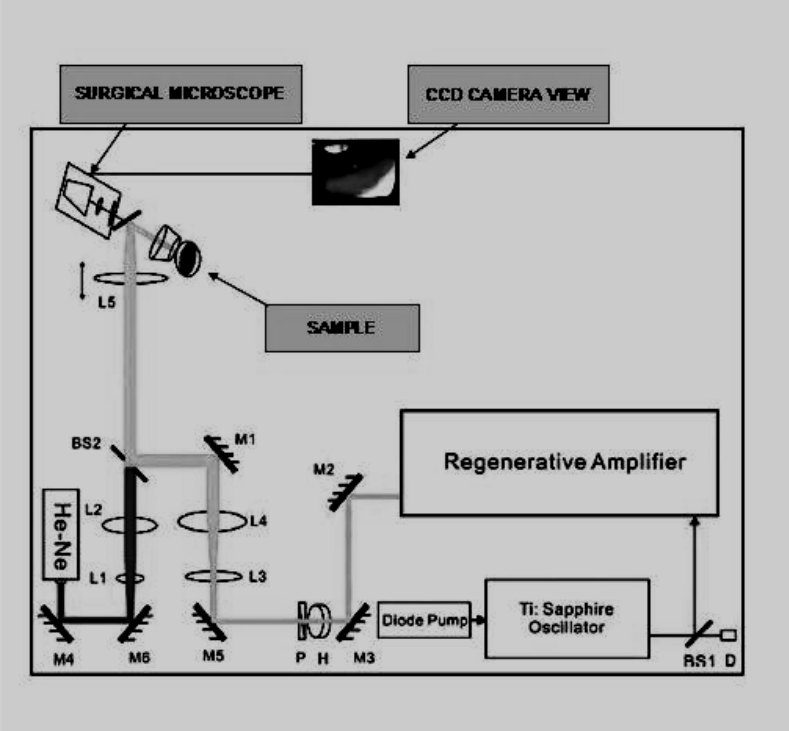

Figure S1. The optical delivery system for ultrafast pulsed laser ablation. M, mirror; BS, beam splitter; L, lens; D, detector; H, half wave plate; P, polarizer; He-Ne, Helium-Neon laser; paths of the guiding and the Ti-Sapphire beams are shown by the sketch. Sample sits in air during ablation.

SEM of individual p-nitroaniline crystals after matrix application for phospholipid analysis showed average crystal sizes were ~20 μm (data not shown). SEM of the sinapinic acid matrix applied for protein analyses showed individual crystal sizes of ~50 μm. The upper mass limit for the MALDI-MS instrument was approximately m/z 13,000. Phospholipid spectra shown are an average of 5,000 laser shots, whereas protein spectra are an average of 20,000 shots. Spectra of phospholipids obtained for comparison of intact tissue surface with the laser ablated

surface were recorded from adjacent MALDI spots located 2.5 mm apart, whereas spectra of proteins were collected from adjacent MALDI spots 3 mm apart. Phospholipid spectra were plotted without any further data processing, whereas protein spectra were smoothed using commercial software (Origin 8.5., OriginLab Corporation, Northampton, MA, USA) by the Savitzky-Golay method with no boundary conditions, 250 points of window, and a second order polynomial smoothing function. Ion intensities were multiplied by a factor of 10, and the baseline was subtracted using a peak-analyzer function that interpolated a baseline of 50 anchor points. An earlier analysis found that the phospholipid composition does not vary significantly across a few mm in the eye lens tissue (Ref. 14). Accordingly, it was expected that phospholipids spectra obtained from adjacent MALDI spots would not differ significantly. Similarly, it was expected that the protein composition would not vary between adjacent MALDI spots belonging to a region of the lens nucleus that had been shown previously to have a uniform protein composition (Ref. 15 and 16). No surface charging was apparent during any MALDI-MS experiments, despite the 300 μm thickness of the tissue slices.

LDPI-MS was collected using a home-built reflectron time of flight mass analyzer, capable of efficient collection of large energy and spatial distributions of ions. The LDPI-MS is equipped with customized pseudo-orthogonal delayed pulsed extraction and acceleration ion optics, a large bore Einzel lens, steering plates, a two-stage ion mirror, and a microchannel plate detector (Ref. 10). Data were acquired by a 12 bit, 125 MS/s plug-in data acquisition card with 128 MS memory (CompuScope 8229, Dynamic Signals LLC, Lockport, IL, USA) using customized software for instrument control (written in LabVIEW VI, National Instruments, Austin, TX, USA). The data acquisition rate was determined by the 10 Hz repetition rate of the Nd:YAG pump laser. Data were collected while the desorption laser was scanned over the tissue

surface at a rate of 0.05 mm/s. LDPI mass spectra shown here are the mean of three consecutively recorded spectra, each of which was an average of 500 individual spectra. Spectra obtained from the intact tissue surface were taken within 2 mm of the laser ablated region. Similar to the MALDI-MS analyses, no surface charging was apparent in the LDPI-MS analysis. In any case, LDPI-MS analyses desorbed neutral species, which are therefore expected to be less sensitive to sample charging effects than MALDI-MS. All spectra were plotted using commercial software (Origin 8.5.), without any further data processing.

SEM of Matrix Crystals on Eye Tissue and MALDI-MS of Eye Tissue.

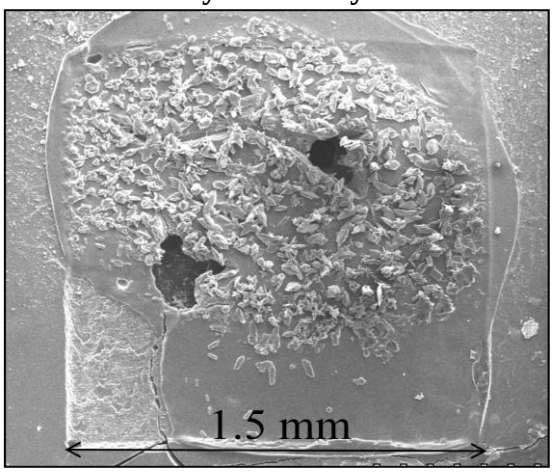

Figure S2. Scanning electron micrograph of bovine eye lens tissue showing ablation patterns and crystals of sinapinic acid matrix. Created by rastering a laser focused to a beam diameter of 200 µm with 10 µm step in a single shot mode using fluence of 0.30 J/cm^2, after matrix application required for subsequent analysis of proteins (×40).

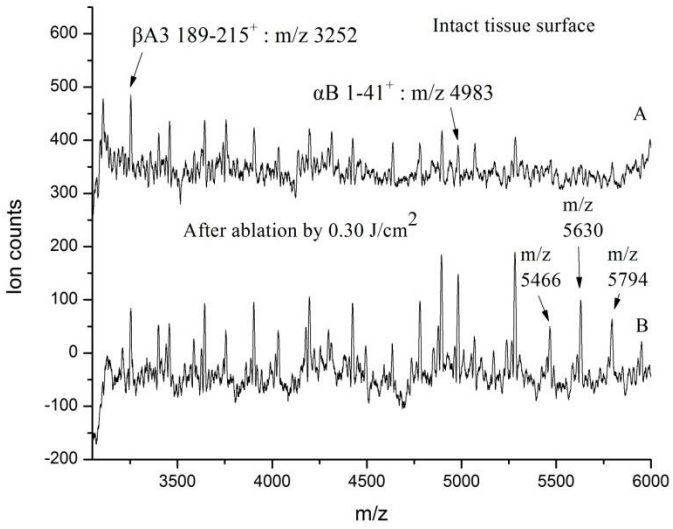

Figure S3. M/z 3000 - 6000 region of MALDI-MS of proteins obtained from eye lens tissue. **A**: intact surface; **B**: after laser ablation by 0.30 J/cm^2.

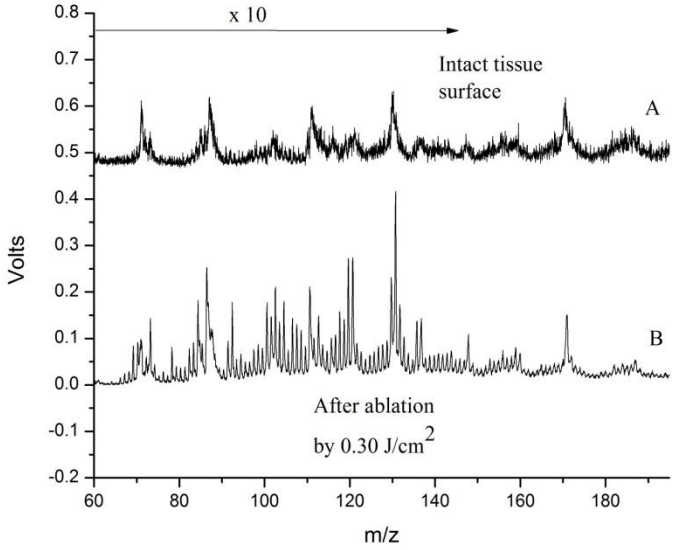

Figure S4. M/z 60 - 195 region of the LDPI-MS of tissue. **A:** intact tissue, peak intensities were multiplied by factor of 10; **B:** after ablation by 0.30 J/cm^2 laser pulses.

Knife Edge Determination of the Effective Beam Spot Size.

The knife edge experiment was conducted in advance of ablation experiments, employing a razor mounted atop of the translational stage and a photodiode mounted behind it. Photodiode signal intensity corresponding to intensity of light passing around the laser blade was recorded as a function of coordinate x perpendicular to the laser beam. The radius of the beam ω_z was obtained after fitting of the data of individual x-scans. All fitting equations were derived from the fundamental relationship of laser fluence dependence of coordinates x and z (across and along the laser beam):

$$\Phi\,(z,x)\;=\;\Phi_0 A e^{\frac{-x^2}{\omega^2}} \qquad \text{(Eq. 1)}$$

where $A = \frac{1}{1+\frac{z^2}{{z_0}^2}}$ and Φ_0 is the peak fluence.

Assuming proportionality between the photodiode signal and the beam energy, the data of individual x-scans was fitted using the relationship of energy and coordinate x derived from Eq. 1:

$$E(\pm x) = \frac{\pi\omega^2\Phi_0}{4}\left[1 \pm \operatorname{erf}\left(\pm\frac{\sqrt{2x}}{\omega}\right)\right] \qquad \text{(Eq. 2)}$$

where $\mathrm{erf}(x) = \frac{2}{\sqrt{\pi}} \int_0^x e^{-z^2}\, dz$, and the radius of the beam ω was corresponding to a point along coordinate x where: $E = \frac{E_0}{e^2}$.

The values obtained for $\omega_z$were plotted as a function of coordinate z and fitted using the relationship between beam radius w_z (defined by e^{-2} point as described) and focal beam radius w_0, coordinate z and the Rayleigh range of the laser beam z_0 using Eq. 3:

$$\omega = \sqrt{\omega_0^2\left(1 + \frac{z^2}{z_0^2}\right)} \qquad \text{(Eq. 3).}$$

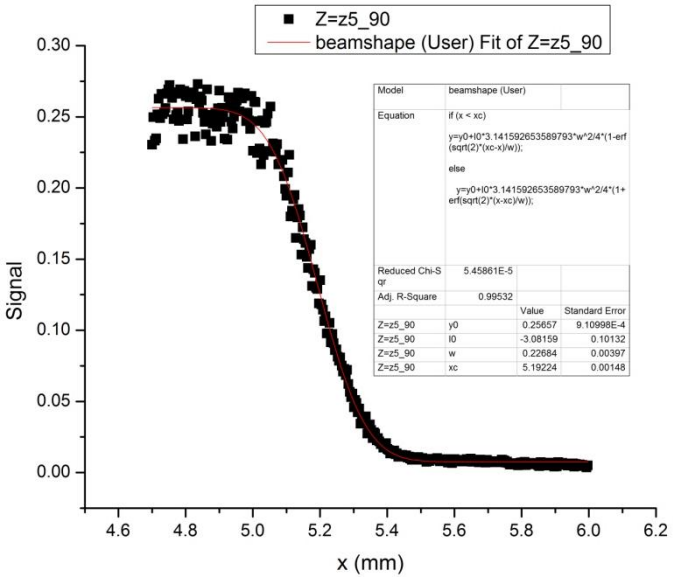

Figure S5. Example of knife edge measurement of laser beam profile. Shown is an individual x-scan of the laser beam (at z = 5.90 mm) showing photodiode signal decrease as a function of x coordinate of the translational stage, fit curve and the numerical results of fitting.

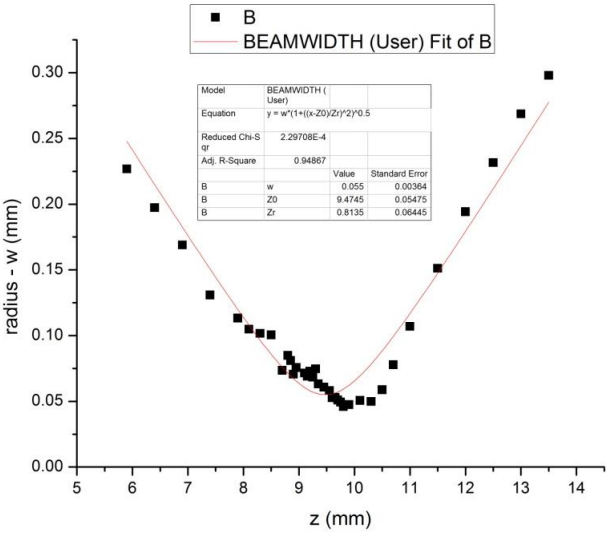

Figure S6. Beam profile from knife edge measurement. Shows dependence of beam radius w_z (defined by e^{-2} point as described) on coordinate*s*, fitting curve and numerical results of the fitting.

To focus a beam above the sample and to select a working beam spot size of 200 μm, the stage was positioned at an appropriate height (*z* coordinate) behind the focal point after accounting for the thickness of the sample.

Determination of Individual Ablation Crater Diameter.

Individual ablation crater size after ablation by fluence of 0.15 J/cm^2 in a raster mode with 10 μm spacing between individual shots was measured by scanning electron microscopic (SEM) imaging of the tissue showing that each ablation crater was well separated from the adjacent craters while each crater was ~10 μm wide.

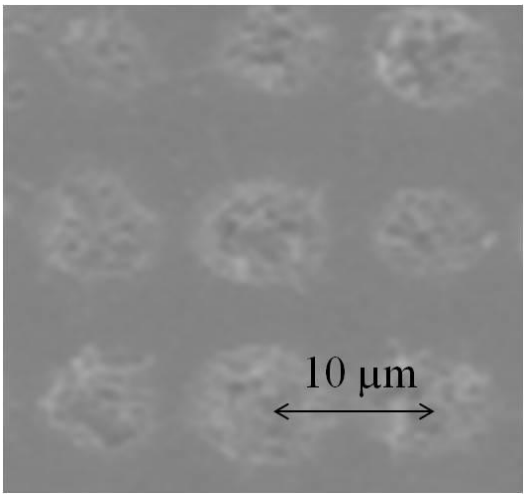

Figure S7. SEM image showing the size of individual ablation craters in eye tissue. Created by fluence of 0.15 J/cm^2 in a raster mode with 10 μm spacing between individual shots.